Chapter 4

Indonesia Case Study description

4.1 TerraSAR-X spacecraft

TerraSAR-X is a German Earth observation satellite that was launched on June 15, 2007 in Baikonur (Kazakhstan) [32]. The partners of the missions are the German Aerospace Center (DLR), the German Federal Ministry of Education and Research and Astrium GmbH. The satellite is controlled from the DLR ground station in Weilheim. Since January 7, 2008, when the mission became fully operational, TerraSAR-X is providing value-added SAR data for scientific, commercial and research-and-development purposes [33].

TerraSAR-X acquires high-resolution and wide-area radar images independent of the weather conditions and presence/absence of sunlight. Its primary payload is an X-band radar sensor with a range of different modes of operation in the X-band [34], allowing it to record images with different swath widths, resolutions and polarizations.

The satellite has a Sun-synchronous circular repeat orbit with a repeat period of 11 days. The orbit has a pre-defined Earth-fixed reference orbit, which closes after a repeat cycle of 167 revolutions in 11 days (its time required to orbit the Earth is 94.85 minutes) [35].

Length	4.88 metres
Diameter	2.4 metres
Launch mass	1230 kilograms
Payload mass	About 400 kilograms

Radar frequency	9.65 Gigahertz
Power consumption	800 watt on average
Orbital altitude	514 kilometres
Rocket	Dnepr 1
Inclination angle with respect to the equator	97.4 degrees
Operational life	At least 5 years an extended lifetime of that least another 5 years (beyond 2018) is expected by the operator DLR

Table 2. Main parameters of TerraSAR-X satellite

The different modes of operation are the Spotlight mode, in which an area of 10 kilometres long and 10 kilometres wide is recorded at a resolution of 1 to 2 metres; the Stripmap mode, which covers a 30-kilometre-wide strip at a resolution between 3 and 6 metres; and the ScanSAR mode, in which a 100-kilometre-wide strip is captured at a resolution of 16 metres [36]. Hence, the use of the sensor can be tailored to the need of the application.

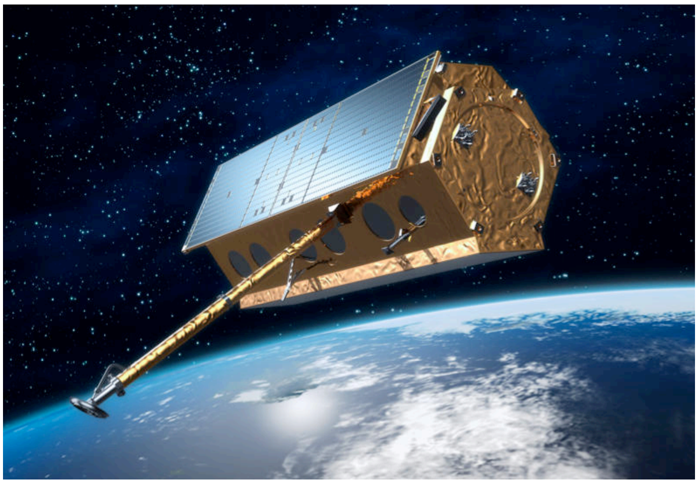

Fig. 10. Artist view of TerraSAR-X satellite

The antenna of TerraSAR-X is an electronically separable Active Phases Array Antenna with a size of 4.78 m x 0.7 m. During nominal operations, the SAR antenna is oriented with an angle of 33.8° degrees off the nadir direction looking right of the flight direction [37]. The antenna allows a variety of polarimetric combinations: single or dual-polarization and even full polarimetric data takes, are possible. Depending on the selected imaging mode there is available one combination or other.

Depending on the desired application, one of four different product types (processing levels) can be selected (Table 3) [37]. All the processing levels are available for the different modes of operation (StripMap, ScanSAR and SpotLight).

Processing Level	Contents
SSC (Single Look Slant Range Complex)	Single look product of the focused radar signal. The data are represented as complex numbers containing amplitude and phase information.
MGD (Multi Look Ground Range Detected)	Detected multi look product with reduced speckle and approximately square resolution cells.
GEC (Geocoded Ellipsoid Corrected)	Multi-look detected product, which is resampled and projected to the WGS84 reference ellipsoid assuming one average height.
EEC (Enhanced Ellipsoid Corrected)	Multi-look detected product, projected and resampled to the WGS84 reference ellipsoid and then corrected using an external Digital Elevation Model (DEM).

Table 3. Processing levels of TerraSAR-X satellite

4.2 TerraSAR-X delivery file format

The TerraSAR-X Basic Image Product is delivered in a standard set of components [38]. One of its components is the annotation information file, provided in xml format, which contains a complete description of the Level 1b product components and is considered as metadata source (provides information about the mission, the acquisition and the orbit, among others). The image channels contain one or more polarimetric channels in separate binary data matrices. These matrices are in the DLR-defined COSAR binary format when the data to deliver is complex and in GeoTiff format when the detected products are delivered.

The set also includes more files, like auxiliary raster files, quicklook images and map plots. The package is supplemented by additional administrative information, which describes the product delivery package and contains additional facility related information (e.g. detailed copyright information), and either archived into a *tar* file or put onto a medium.

4.3 Description of the Indonesia dataset

The dataset used in this thesis covers an area of Pangkalan Bun (Figure 11), a town in Central Kalimantan Province, Indonesia and was taken on 13th March, 2008. Its acquisition mode is TerraSAR-X StripMap and the processing level is SSC (Single Look Slant Range Complex), hence the image channel is in CoSAR format. It has dual-polarization mode and an incidence angle of 33.7º.

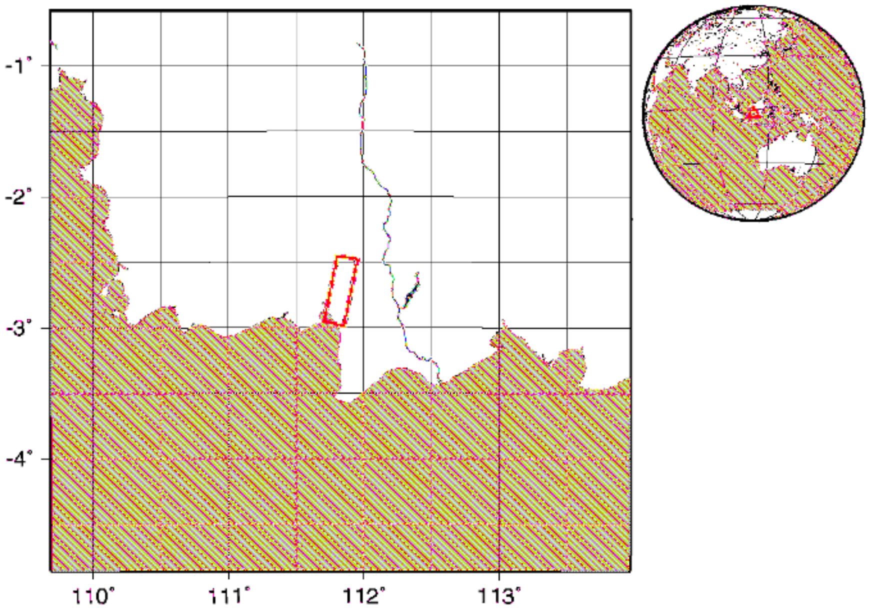

Fig. 11. Map of the area covered by the Case Study dataset

Some of the characteristics of the dataset are shown in Table 4.

Number of rows (ground range)	23361
Number of columns (azimuth)	10288
Image data format	CoSAR
Image data depth	32 meters
Polarization mode	HH-VV (dual-pol)
Ground range resolution	2.12 metres
Azimuth resolution	6 meters
Start time UTC	2008-03-13T22:19:55.140975
Stop time UTC	2008-03-13T22:20:03.140925

Table 4. Characteristics of the TerraSAR-X Indonesia dataset

Due to the large area that the SAR image covers and the high computational demand that this implies, three different subareas (Figure 12) of the main dataset are selected to carry out the overall process of decomposition and classification. Working with different subareas also allows to check that the obtained results of the classification algorithm are independent of the input data. The selected subareas have some interesting zones for the posterior classification, like water, different types of vegetation and ships.

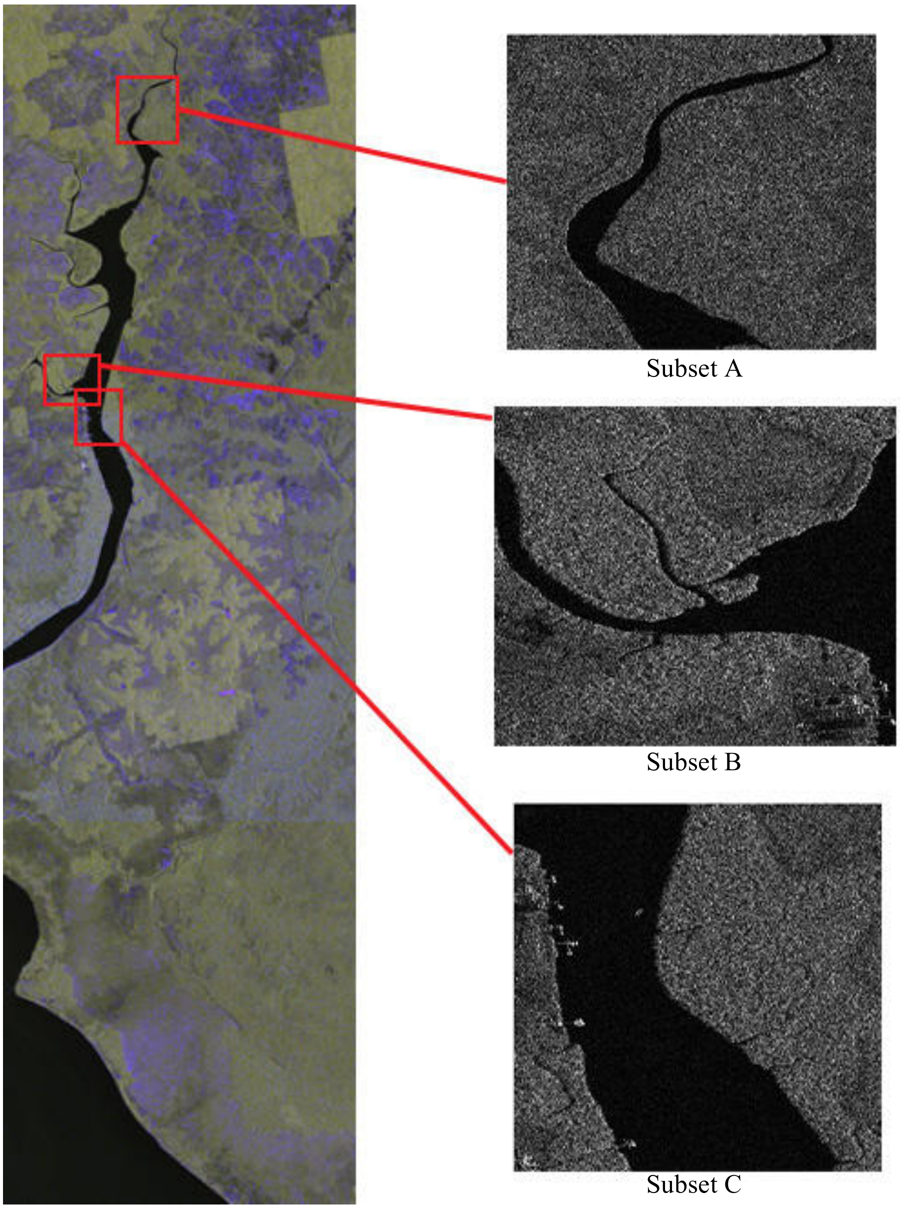

Subset A

Subset B

Subset C

Fig. 12. Reconstruction image of the entire dataset and HH channels of the three selected subsets

Figure 13 shows in detail the three subsets chosen for the analysis and segmentation, relating its HH channel matrix image with an aerial image of the same area captured by Google Earth. Note that the quality of Google Earth image in subset C is quite poor, fact that difficults the identification of each target. Also note that the HH-channel image seems a little deformed since its resolution in azimuth and in range are not the same.

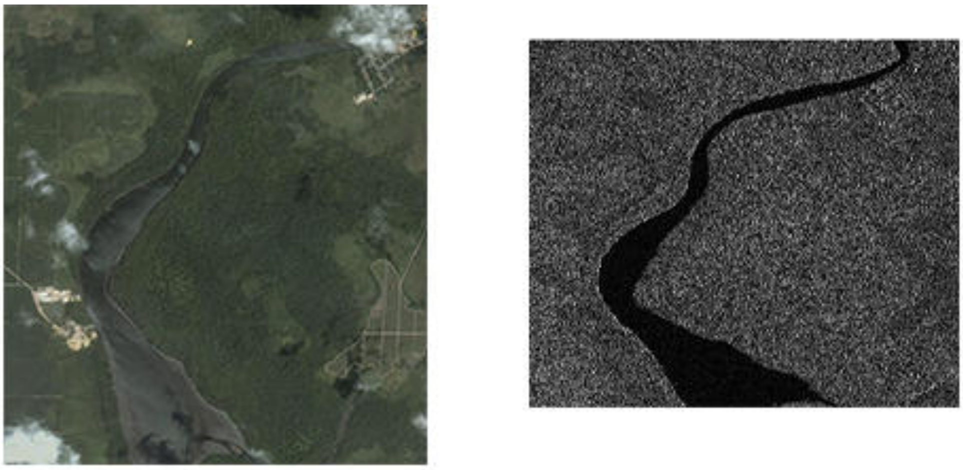

Subset A

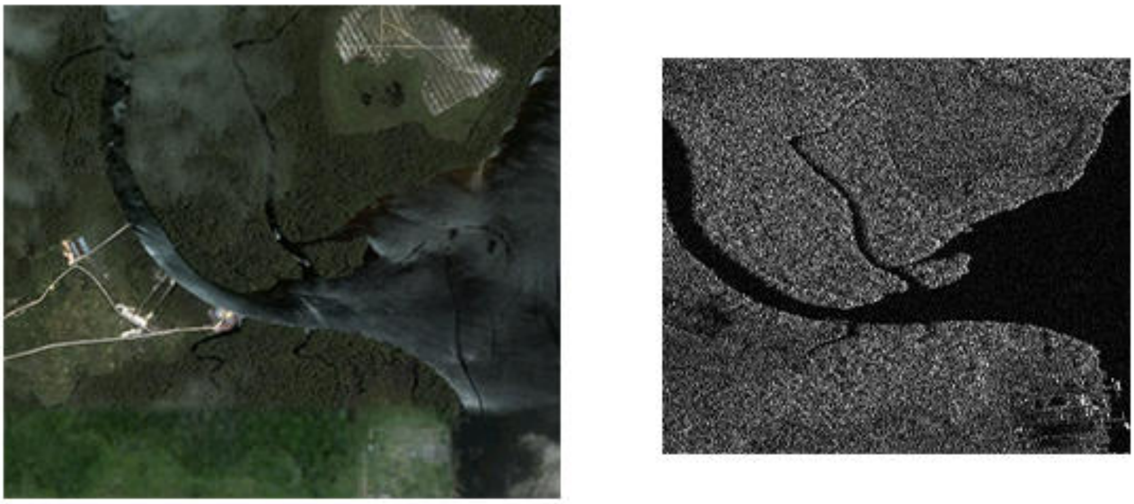

Subset B

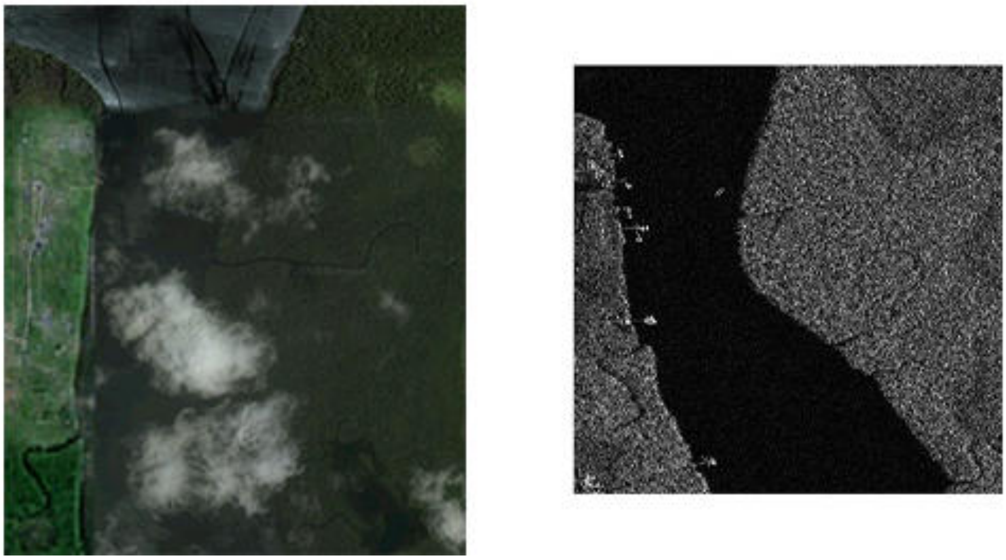

Subset C

Fig. 13. Aerial image of the three subsets captured by Google Earth and their corresponding HH channel matrix image.

Chapter 5

H-α Decomposition applied to the Case Study

5.1 Theory of H-α Decomposition

Polarimetric decompositions are techniques used to generate polarimetric discriminators that can be used for analysis, interpretation and classification of SAR data [39]. These techniques allow the information extraction of the scattering processes that involve a specified target. There are two types of polarimetric decompositions; one is coherent decomposition, which is based in the decomposition of the scattering matrix, while the other, called incoherent decomposition is based in the decomposition of the coherency or covariance matrices [40]. H-α decomposition is an incoherent decomposition that analyzes the power form (the coherency matrix in this case) of the scattering matrix.

H-α decomposition is an entropy based decomposition method for quad polarization data proposed by Cloude and Pottier on 1997 [30]. This method is based on the hypothesis that the polarization scattering characteristics can be represented by the space of the entropy and the averaged scattering angle α by means of the eigenvalue analysis of Hermitian matrices. The H-α decomposition does not rely on the assumption of a particular underlying statistical distribution and so is free from the physical constraints imposed by such multivariate models. This method has such good properties as rotation invariance, irrelevance to specific probability density distributions and the coverage of the whole scattering mechanism space.

In this thesis dual-polarization (HH and VV) SAR data is used, so the H-α decomposition method has been extended in order to be applied to this data type.

5.1.1 Extraction of the H-α parameters

For the extraction of the entropy (H) and the alpha (α) parameters the coherency matrix explained in the Chapter 4 is needed. Remember that each pixel of the dual-polarization SAR data represents a 2 x 2 coherency matrix $[T_2]$, which is nonnegative, definite and Hermitian.

$$[T_2] = \begin{bmatrix} T_{11} & T_{12} \\ T_{21} & T_{22} \end{bmatrix} = \begin{bmatrix} T_{11} & T_{12} \\ T^*{}_{12} & T_{22} \end{bmatrix} \tag{21}$$

As mentioned previously, the H-α decomposition is computed by means of the eigenvalue analysis, so in (22), (23) and (24) the eigenvalue decomposition of the coherency matrix is done [30].

$$[T_2] = \begin{bmatrix} T_{11} & T_{12} \\ T_{21} & T_{22} \end{bmatrix} = U \begin{bmatrix} \lambda_1 & \\ & \lambda_2 \end{bmatrix} U^H = \lambda_1 u_1 u_1^H + \lambda_2 u_2 u_2^H \tag{22}$$

$$U = \begin{bmatrix} u_{11} & u_{12} \\ u_{21} & u_{22} \end{bmatrix} = [u_1 \quad u_2] \tag{23}$$

$$u_i = e^{j\phi_i}[\cos\alpha_i \quad \sin\alpha_i e^{j\delta_i}]^T \tag{24}$$

The subscript *H* denotes the Hermitian matrix, which is the conjugate transpose, so U^H is equivalent to U^{*T}.

Once the eigenvalues λ_1 and λ_2 and the eigenvectors u_1 and u_2 of the coherency matrix have been obtained, it is possible to compute the entropy H (25), which defines the degree of statistical disorder of each distinct scatter type within the ensemble, and the alpha α (26), which is related directly to underlying average physical scattering mechanism and hence may be used to associate observables with physical properties of the medium [41].

$$H = \sum_{i=1}^{2} -P_i \, log_2 \, P_i \tag{25}$$

$$\alpha = \sum_{i=1}^{2} P_i \, cos^{-1}(|u_{1i}|) \tag{26}$$

where P_i (27) correspond to the pseudo-probabilities obtained from the eigenvalues λ_1 and λ_2. Since the eigenvalues are rotational invariant, the entropy H and the alpha α are also roll-invariant parameters.

$$P_i = \frac{\lambda_i}{\sum_{j=1}^{2} \lambda_j}, \quad i = 1, 2 \tag{27}$$

Computing the preceding equations for the whole coherency matrix results in the entropy and alpha matrices, which have the half size of the coherency matrix due to for each group of 2x2 pixels in the coherency matrix, one value of entropy and one value of alpha are obtained. The entropy values are between 0 and 1, where a high value involves higher entropy in the pixel in question. The values of the alpha are between 0 and 90 degrees.

5.1.2 Interpretation of H-α feature space

The H-α plane is divided into nine basic regions characteristic of different scattering behavior, as shown in Figure 14 [30]. The basic scattering mechanism of each pixel of a polarimetric SAR image can be identified by comparing its entropy and α parameters to fixed thresholds. The location of the boundaries of the regions is set based on the general properties of the scattering mechanisms, but they can be modified to fit a particular dataset.

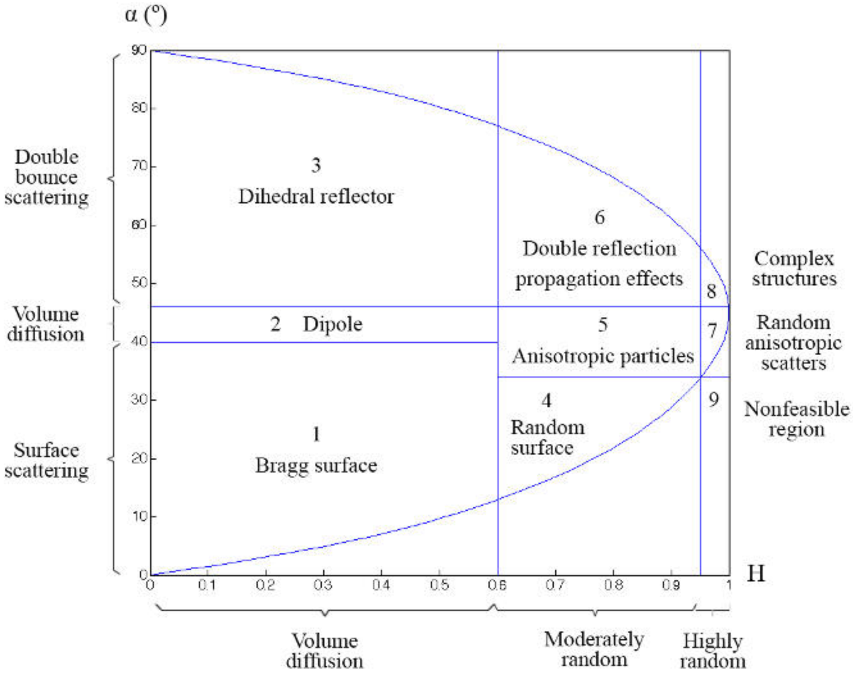

Fig. 14. H-α classification plane

Table 5 shows the typical scattering mechanism of each of the nine zones of the H-α feature space as well as its boundaries. Each zone is represented with a different color that will be useful for the results representation in Chapter 5.3.

Zone	Color	Scattering mechanism	Boundaries
1	🟥	Low entropy surface scattering	Alpha <= 40 and H <= 0.6
2	🟦	Low entropy dipole scattering	40 < Alpha <= 46 and H <= 0.6
3	🟧	Low entropy multiple scattering	Alpha > 46 and H <= 0.6
4	🟩	Medium entropy surface scattering	Alpha <= 34 and 0.6 < H <= 0.95
5	⬛	Medium entropy vegetation scattering	34 < Alpha < 46 and 0.6 < H <= 0.95
6	🟦	Medium entropy multiple scattering	Alpha >= 46 and 0.6 < H <= 0.95
7	🟪	High entropy vegetation scattering	34 < Alpha < 46 and H > 0.95
8	🟨	High entropy multiple scattering	Alpha > 46 and H > 0.95
9		High entropy surface scattering (nonfeasible)	Alpha <= 34 and H > 0.95

Table 5. Zones of H-α feature space

The different boundaries in the H-α plane discriminate between surface reflection, volume diffusion and double bounce reflection along the α axis and low, medium and high degree of randomness along the entropy axis [30]. Surface scattering is characteristic for agriculture fields, bare soils, flat surfaces and calm water, volume diffusion appears mainly over forested areas and double bounce scattering is typical for urban areas and buildings.

The alpha angle varies between 0° and 90° and allows the identification of the type of scattering process. If $\alpha = 0°$, the scattering is related to plane surface, whereas for $\alpha = 45°$, the result shows the scattering characteristics are those of a dipole. Between $\alpha = 0°$ and $\alpha = 45°$, it results in an irregular surface and for $\alpha = 45°$ to $\alpha = 90°$ the response is the result of a double bounce scatterer.

Lower values for entropy means that it is easier to extract information from the scattering. A higher value for entropy indicates that there are more than one scattering mechanisms and that they are equal in strength [42]. So, there is an increasing disability to differentiate scattering mechanisms as the entropy increases. If the entropy is close to zero, the alpha angle gives the dominant scattering mechanism for that resolution cell i.e., scattering is volume, surface or double bounce. Entropy increases as a natural measure of the inherent reversibility of the backscatter data; hence it can be used for identification of underlying scattering mechanism.

5.2 Application of H-α Decomposition to the Case Study

The data flow diagram for the work carried in Matlab out using the Indonesia dataset is illustrated in Figure 15.

Fig. 15. Overall data flow diagram for the Case Study

The data flow has been applied to the three subsets of the Indonesia dataset and the results are shown in the Chapter 5.3.

5.3 Decomposition results of the Case Study

According to the flow diagram of Figure 15, the input dual-polarized COSAR Indonesia dataset has been read to extract separately the HH-channel and VV-channel matrices (Figure 16). Although the process has been applied to the three subsets of the Indonesia dataset, for the firsts steps it is shown only the subset A.

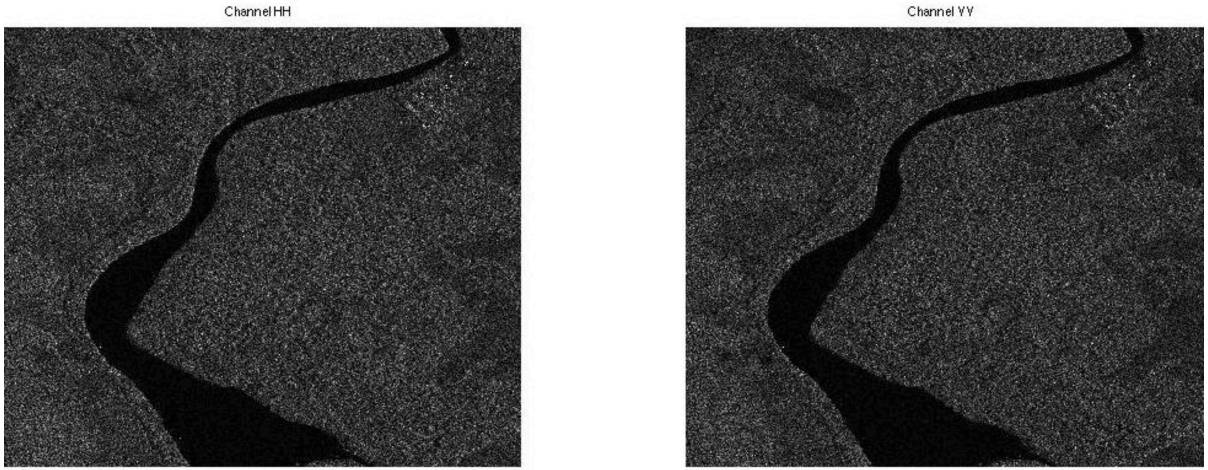

(a) **(b)**

Fig. 16. Polarimetric channels of the subset A: (a) HH-channel, (b) VV-channel

The calm river water appears like a dark area in the SAR images since most of the incident radar pulses are specularly reflected away so very little energy is scattered back to the radar sensor. Forests and vegetation are usually moderately rough on the wavelength scale. Hence, they appear as moderately bright features in the SAR image. In the right-top corner of Figure 16 very bright targets appear, which indicates double-bounce effect where the radar pulse bounces off the horizontal ground towards the target and then the pulse is reflected from one vertical surface of the target back to the sensor. It happens because in this zone there are some buildings.

Once the HH-channel and VV-channel have been extracted, a square multilook window of five pixels has been applied in order to reduce the speckle noise that appears often is SAR images and create a more homogeneous image. The speckle noise is formed from coherent summation of the signals scattered from ground scatterers distributed randomly within each pixel.

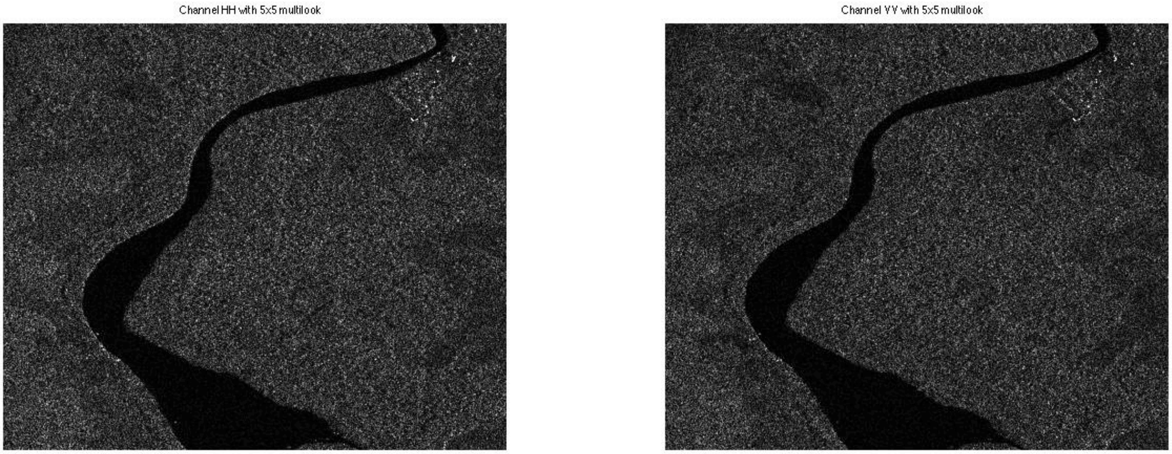

(a) (b)

Fig. 17. Polarimetric channels of the subset A with 5x5 multilook window: (a) HH-channel, (b) VV-channel

After applying the speckle removal filter (Figure 17) there is not appreciated a substantial visual improvement in the image quality regarding the unfiltered input; however, for the computation of the coherency matrix this step is mandatory since it can considerably affect to the final results.

Once the multilooked HH-channel and VV-channel have been obtained, the coherency matrix, which will be fundamental for the H-α decomposition, is computed. With the obtained coherency matrices (one for each subset), the H-α decomposition explained in 5.1 can be applied to the three different subsets of the Indonesia dataset.

- **Subset A**

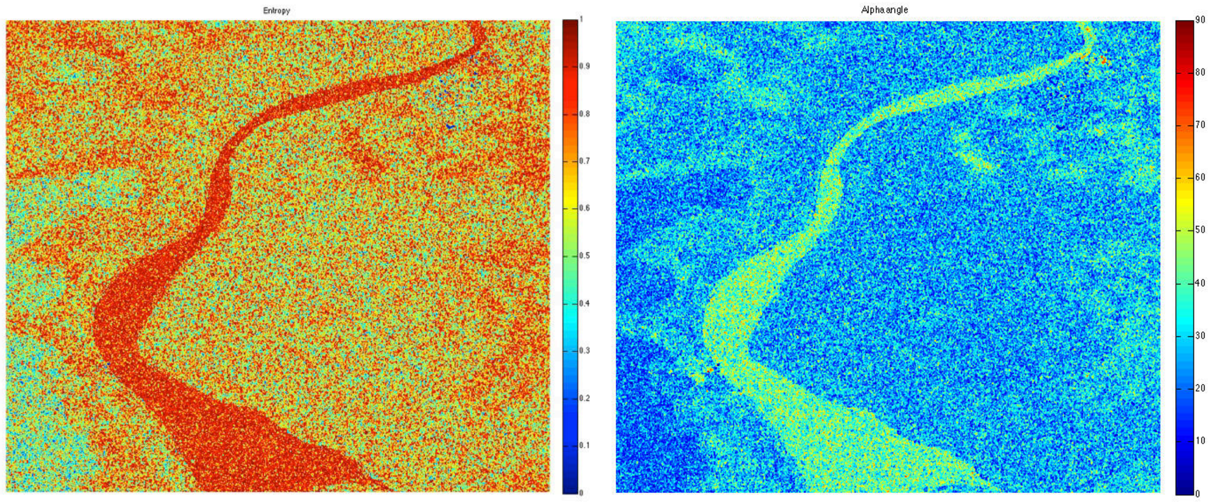

(a) **(b)**

Fig. 18. Parameters extracted from the subset A: (a) entropy, (b) alpha angle

In Figure 18.a the entropy of the subset A is shown. The highest values of entropy appear in the river and in some areas of the forest (mainly located at the right of the image). For smooth river surfaces, with little or no relief at the scale of the radar wavelength, there is little return energy as the incident wave undergoes specular reflection. These areas are associated with high alpha and high entropy, indicating that very low amplitude backscatter is mainly random noise. Forest areas with high entropy appear since they are areas with more sparse vegetation and dryer than the rest of the forest. In areas of dry soil some of the incident radar energy is able to penetrate into the soil surface, resulting in less backscattered intensity. The rest of the forest, occupying the main part of the image, has medium entropy due to the increased density of vegetation in a uniform way. The zones with the lowest values of entropy appear in the left of the image where there are some crops. Those crops follow a more ordered and homogeneous structure than the forests, which entails in lower values of entropy.

In Figure 18.b the alpha angle of the subset A is shown. Medium-high alpha values appear in the river and some forests zones (the same areas that have the highest values of entropy) as a volume diffusion mode. The crops have the lowest alpha (with values lower than 30 degrees), which indicates surface scattering. In the top right of the image as well as in the bottom left, there are some very high alpha values due to in these zones there are some buildings with medium height (Figure 19.a and 19.b) that generates double bounce scattering, so the radar beam bounces twice off the ground and the wall surfaces and most of the radar energy is reflected back to the radar sensor.

(a) **(b)**

Fig. 19. Zoom of the zones with the highest alpha in subset A produced by the yellow buildings.

The corresponding H-α plane for the subset A is represented in Figure 20.

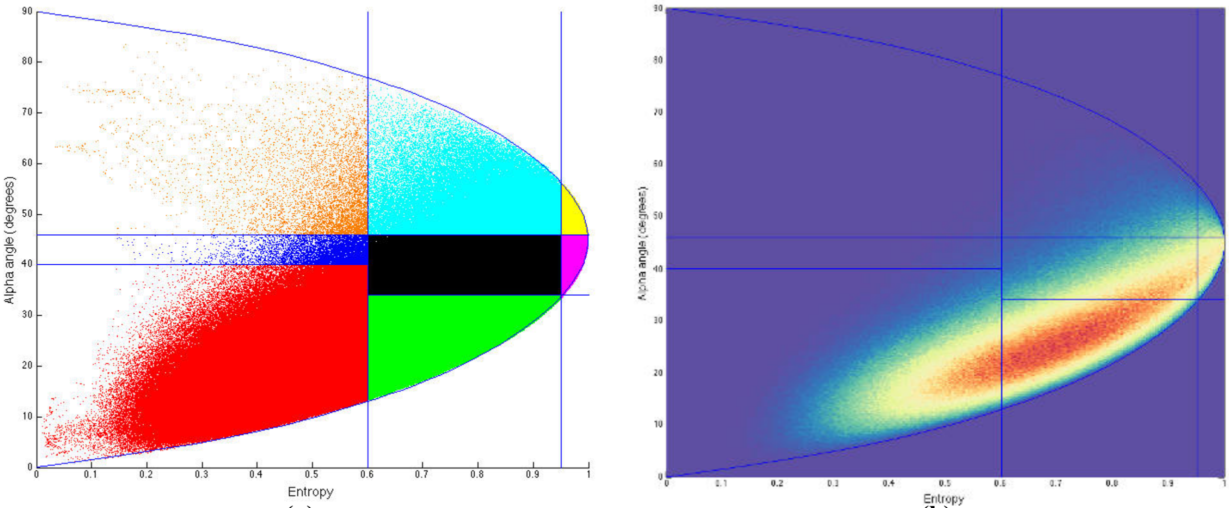

(a) **(b)**

Fig. 20. H-α plane of the subset A: (a) zones with diferent colors, (b) density plot of the plane

Each of the nine zones of the H-α plane has been represented with their corresponding color according to Table 5 (Figure 20.a). This will allow doing a first classification of the subset depending on the zone to which each pixel belongs (Figure 21). A density plot for the H-α plane is shown in Figure 20.b since it is difficult to visually determine in which areas there is more density of pixels. The color of each point of the density plot represents the frequency of pixels within that region of the grid, which enables to visualize which are the more characteristic scattering mechanisms of the terrain.

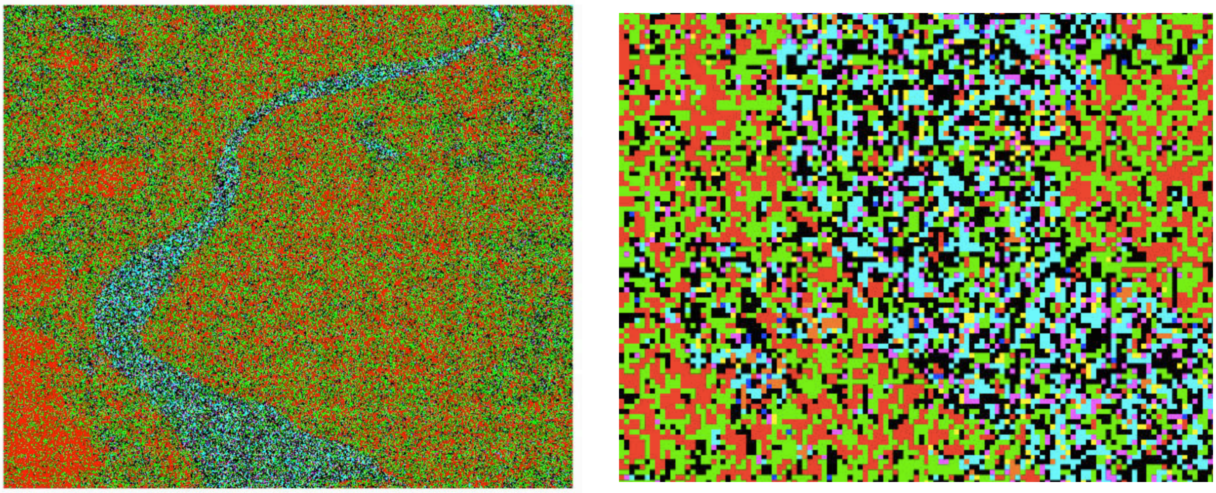
(a) (b)

Fig. 21. Subset A classified using H-α plane: (a) subset A, (b) area of subset A in detail

The water of the river is mainly classified as medium entropy multiple scattering zone, as well as some areas in the top right corner that also had the higher image entropy values compared with the rest of the forest. When the classified image is seen in more detail (Figure 21.b) some pinky areas appear in the river, which correspond to even higher entropy due to the randomness caused by the water surface. The general part of forest in the image is a combination of medium entropy surface scattering and low entropy surface scattering, while the crops (at the left of the image) appear more clearly as low entropy surface scattering class due to the homogeneity of the area. The regions with buildings (Figure 19) are classified as low entropy multiple scattering zones (dihedral reflectors) due to the double bounce effect of the radar wave.

- **Subset B**

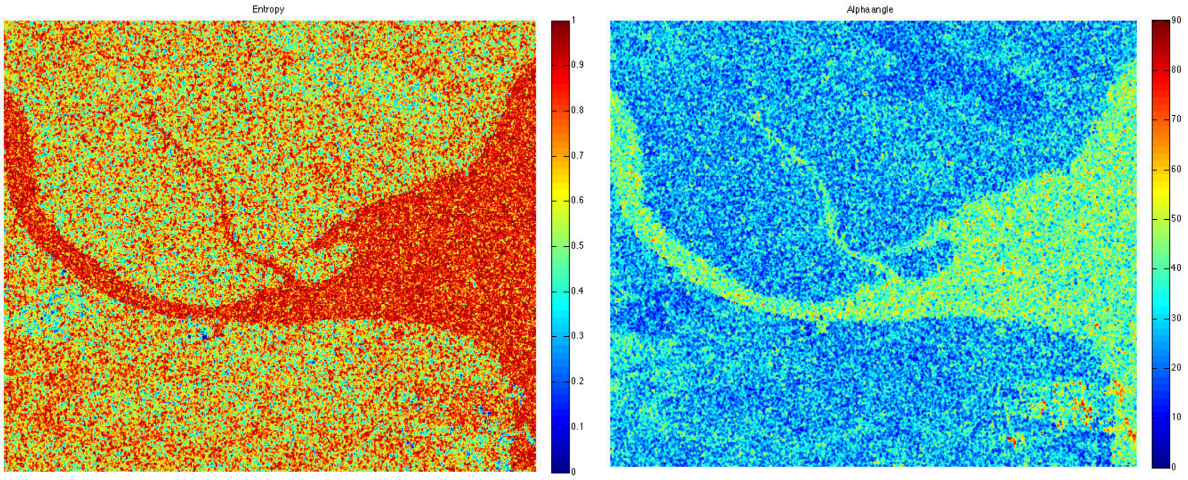

(a) (b)

Fig. 22. Parameters extracted from the subset B: (a) entropy, (b) alpha angle

In both Figures 22.a and 22.b the main forest and the water of the river behaves in a similar way than in the subset A; so in the water appears the highest entropy due to the smoothness of the surface causes specular reflection while in the forest there is a medium value of entropy. Unlike in subset A, near the top center and the left center of the subset B there are some forest areas with lower value of entropy, which indicates that the soil in this area is wetter so the large difference in electrical properties between water and air results in higher backscattered radar intensity. At the bottom right of subset B there is a zone with very low entropy and very high alpha referred to an area of buildings that generate a double bounce response.

The corresponding H-α plane for the subset B is represented in Figure 23.

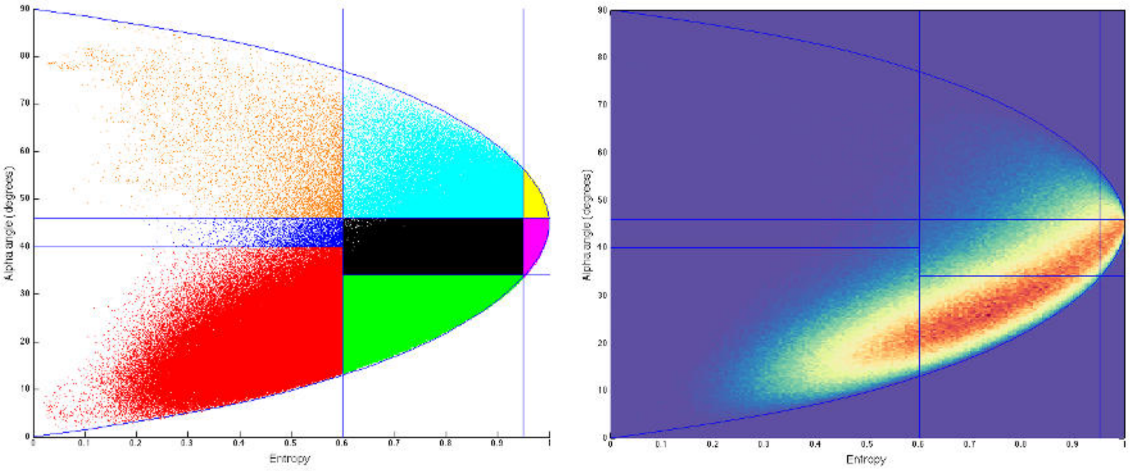

(a) **(b)**

Fig. 23. H-α plane of the subset B: (a) zones with diferent colors, (b) density plot of the plane

Both figures (23.a and 23.b) are very similar to the ones of the subset A due to the similarity of the terrain. In Figure 23.b can be appreciated that the zone 8 has more density of pixels than the set A due to the higher quantity of river.

A first classification of the subset B according to the zone to which each pixel belongs in the H-α plane is shown in Figure 24. The classification of the subset B follows a similar structure than in the subset A, so the water of the river is classified as medium entropy multiple scattering zone and the general part of forest is classified as a combination of medium entropy surface scattering and low entropy surface scattering. The previously mentioned wet areas of the forest appear more clearly as low entropy surface scattering class. The regions with buildings at the bottom right of the subset B are classified as low entropy multiple scattering zones due to the double bounce scattering mechanism at this area.

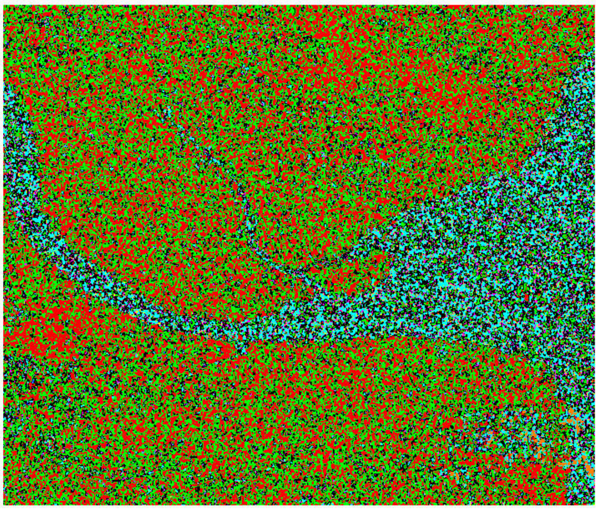

Fig. 24. Subset B classified using H-α plane

- **Subset C**

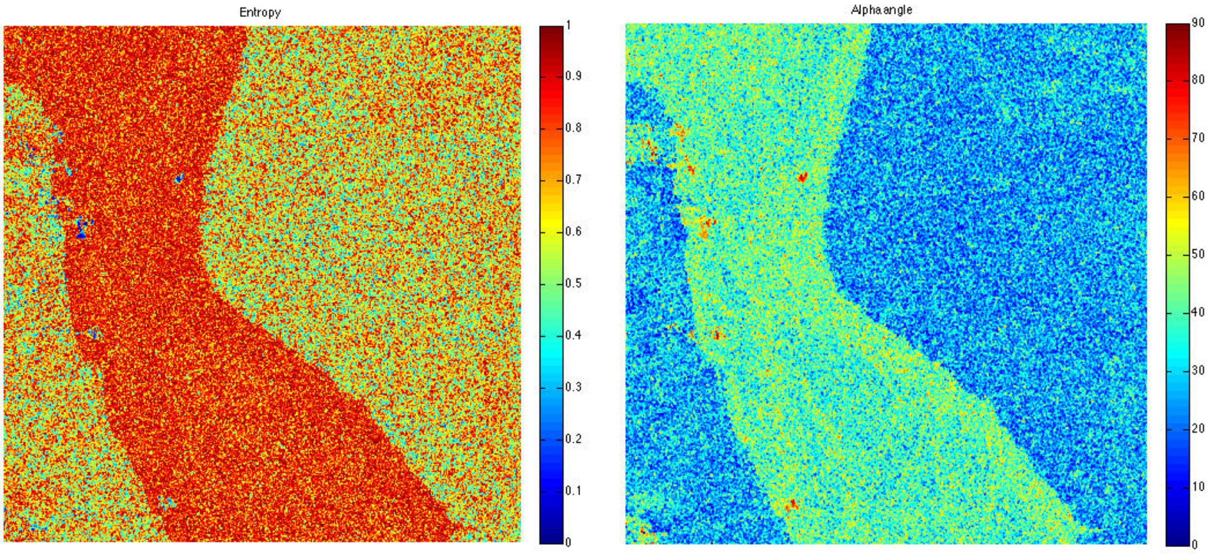

(a) **(b)**

Fig. 25. Parameters extracted from the subset C: (a) entropy, (b) alpha angle

In both Figures 25.a and 25.b the forest and the water of the river behaves again in the same way than in the subset A (in the water appears the highest entropy values while in the forest there is a medium value of entropy). There are some clearly visible ships mainly on the left side of the river that are classified as targets with very low entropy and very high alpha due to the double bounce effect of the radar wave.

The corresponding H-α plane for the subset C is represented in Figure 26. Both subfigures (Figure 26.a and Figure 26.b) are very similar to the ones of the subset A and B, although in Figure 26.b it can be appreciated that the zone 7 has more density of pixels than in the subset

B due to in this case the river, which has pixels with high entropy, occupies approximately a half part of the image.

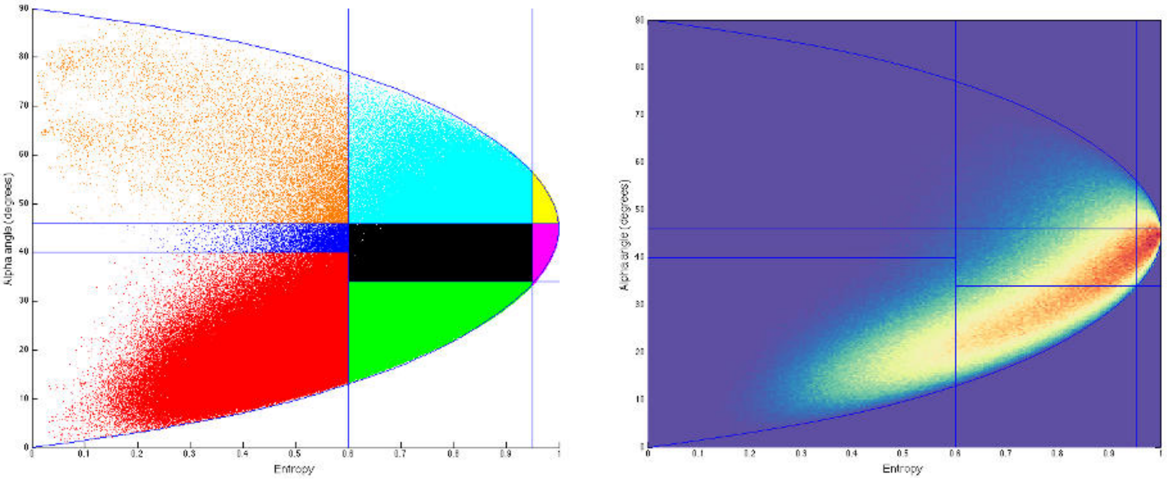

(a) (b)

Fig. 26. H-α plane of the subset C: (a) zones with diferent colors, (b) density plot of the plane

A first classification of the subset C according to the zone to which each pixel belongs in the H-α plane is shown in Figure 27.

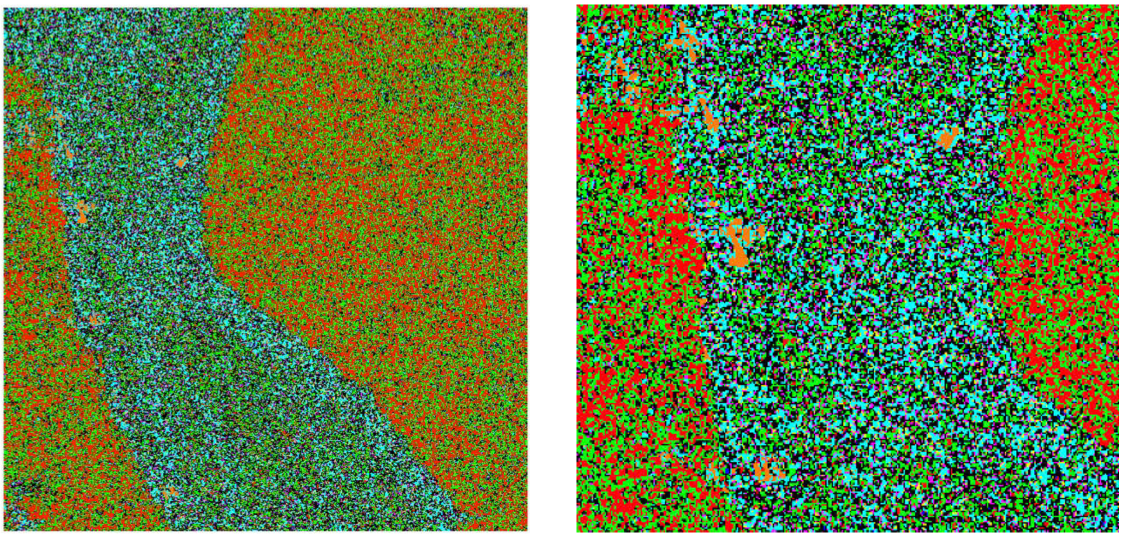

(a) (b)

Fig. 27. Subset C classified using H-α plane: (a) subset C, (b) area of subset C in detail

The classification of the subset C follows again a similar structure than the subset A and B, being the water of the river classified as medium entropy multiple scattering zone and the forest as a combination of medium entropy surface scattering and low entropy surface scattering. The ships on the river are easily distinguishable over the water and are clearly classified as low entropy multiple scattering targets (dihedral reflectors) due to the generated double bounce of the wave.

These first classifications of the three subsets based on the resulting H-α plane zones of each pixel of the images give an initial idea of the different image areas, but the resulting areas mainly are a combination of two or more classes so it results in noisy classification images with heterogeneous regions. Hence, in the next Chapter a classification algorithm is going to be applied to these first classification images in order to segment more properly the initial SAR data and achieve more homogenous zones.

Chapter 6

Wishart classifier applied to the Case Study

6.1 Supervised and unsupervised terrain classfication

Terrain and land-use classifications are probably the most important applications of polarimetric synthetic aperture radar (PolSAR). Supervised and unsupervised terrain classification can be reached by means of many developed algorithms. In supervised classification, training sets for each class are used, based on ground truth maps or scattering contrast differences in PolSAR images. In unsupervised classification the image is classified automatically by finding clusters based on a certain criterion [43]. However, the final class identification may have to be inferred manually.

Unsupervised classification methods are divided into three different categories [44]; the first only takes into account the statistical characteristics of SAR data (ignoring the physical scattering mechanisms of the media), the second classifies by inherent physical scattering characteristics (ignoring the statistical property) and the third both the statistical property and its physical scattering characteristics are combined. The second method has the advantage relative to the first of providing information for class type identification.

In Chapter 5.3 has been shown the results of the classification proposed by Cloude and Pottier based on their target decomposition theory (Chapter 5) using the scattering mechanisms characterized by entropy H and alpha α angle. This classification uses the H-α plane divided into eight zones where the entropy and alpha associated with each zone provides information for terrain type assignment [6]. The problem of this method appears due to the zone boundaries in the H-α plane are preset and the clusters may fall on a boundary or more than one class may be enclosed in a zone.

In this thesis an algorithm proposed by Lee et al. has been developed, which is a combination of the unsupervised H-α decomposition classifier and the supervised Wishart classifier [6]. This algorithm uses the classification result of the Cloude and Pottier unsupervised classification [30] as input to the Wishart method.

6.2 Wishart classifier algorithm

As has been mentioned in Chapter 6.1, Wishart classifier algorithm uses the initial Cloude and Pottier classification map as training set for iterative Wishart classification [45]. The algorithm is formed for three main steps; first of all, the cluster center of coherency matrices, V_i, is computed for pixels in each zone using the initial classification map (28):

$$V_i = \frac{1}{n_i}\sum_{j=1}^{n_i} \langle T \rangle_j, \text{ for all pixels in class } \omega_i \tag{28}$$

where $\langle T \rangle$ is the spatial averaged coherency matrix and n_i is the total number of pixels in each class. With this equation eight cluster centers are obtained, one for each class.

Once the clusters have been obtained each pixel is reclassified by applying the Wishart distance measure for the coherency matrix (29):

$$d(\langle T \rangle, V_m) = ln|V_m| + Tr(V_m^{-1}\langle T \rangle) \tag{29}$$

where $d(\langle T \rangle, V_m)$ is the distance to the cluster V_m and $\langle T \rangle$ is again the spatial averaged coherency matrix. For each coherency matrix eight distances are obtained, one for each cluster, and each pixel is then classified to the cluster with the lowest distance. Once the image is reclassified the result is then used to update the clusters, V_i, and reclassify the image again [46]. The iterating process stops when the number of pixels switching class becomes smaller than a predetermined number, or a termination criterion is met.

6.3 Application of the Wishart classifier to the Case Study

The data flow diagram for the Wishart classification carried in Matlab out using the Indonesia dataset is illustrated in Figure 28.

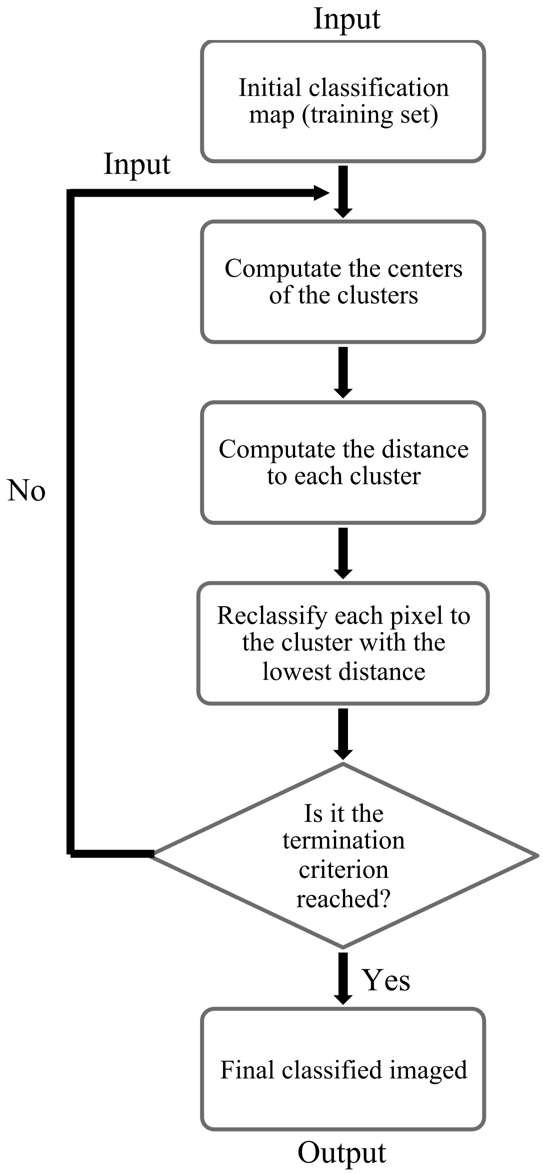

Fig. 28. Data flow diagram of the Wishart classifier

The data flow has been applied to the three subsets of the Indonesia dataset and the results are shown in the Chapter 6.4.

6.4 Classification results of the Case Study

According to the flow diagram of Figure 28 and as it has been said in Chapter 6.1, the input of the Wishart classifier is the classification map obtained in Chapter 5.3 with the H-α plane and it is used for the first iteration of the algorithm. Those initial classification maps (one for each subset of the Indonesia dataset) are shown in Figure 21 (subset A), 24 (subset B) and 27 (subset C).

- **Subset A**

According to the flow diagram of Figure 28, the first step is the computation of the centers of the clusters of the initial classification map. Those centers have been ploted on the density H-α plane obtained in Chapter 5.3 and are shown in Figure 29.

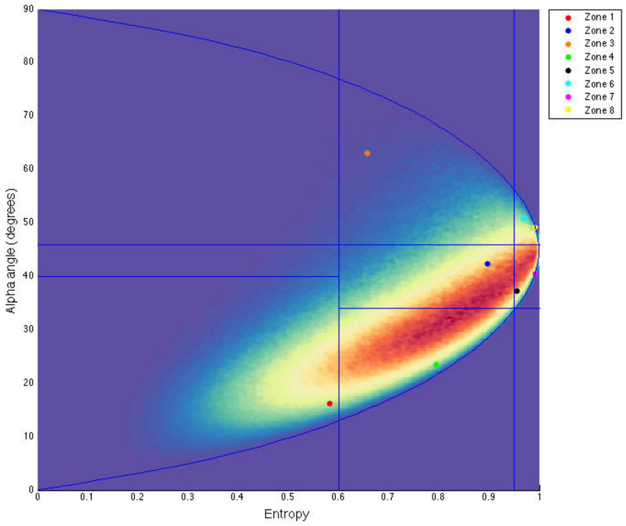

Fig. 29. Cluster centers of the initial classification map of the subset A.

The clusters centers have been computed using the coherency matrix and it is appreciated in Figure 29 that the centers are close to the region with more density of pixels. The centers of the clusters of the zones with less density of pixels can appear in other zones due to the centers have been computed using the coherency matrix and not the H-α plane.

With the centers of the clusters, according to the flow diagram of the Figure 28, the Wishart distance is computed to reclassify each pixel to the cluster with lowest distance. The result of the first iteration of the Wishart classifier is shown in Figure 30.a.

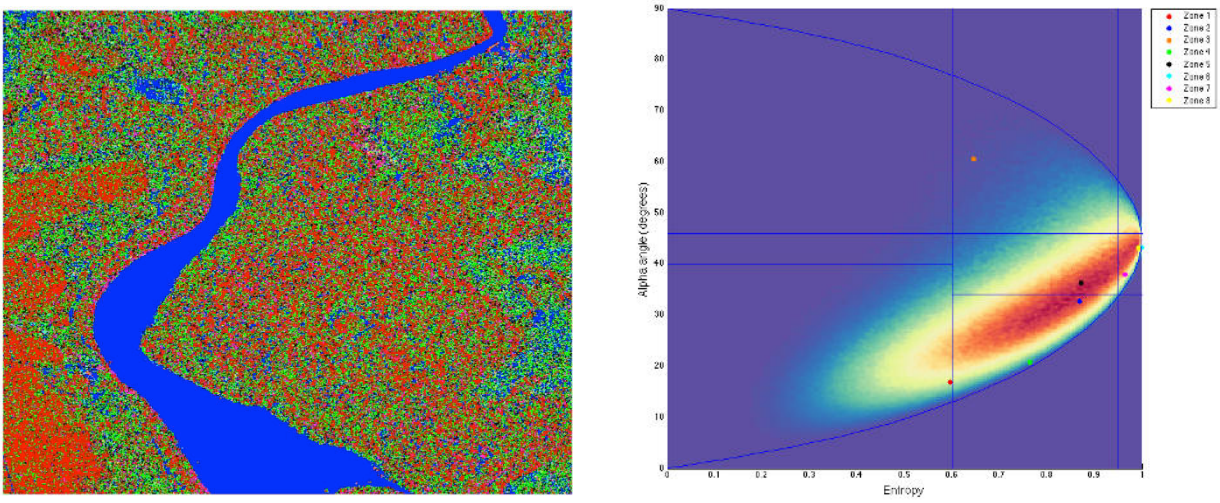

(a) (b)

Fig. 30. First iteration of the subset A: (a) classified image, (b) cluster centers

Figure 30.a shows the result of the first iteration of the Wishart classifier. Compared with the initial classification map obtained with the H-α plane (Figure 21) the different zones of the image (forests, river, crops) are now much more differentiated, mainly the river, which has been fully classified as low entropy dipole scattering.

Due to the resulting classified image has a considerable improvement, the termination criterion has not been met and this resulting image is now used as training set for the second iteration of the Wishart classifier. In Figure 30.b the centers of the clusters of the first iteration are shown and they are even closer to the region with more density of pixels. In addition, some clusters centers have changed its zone again.

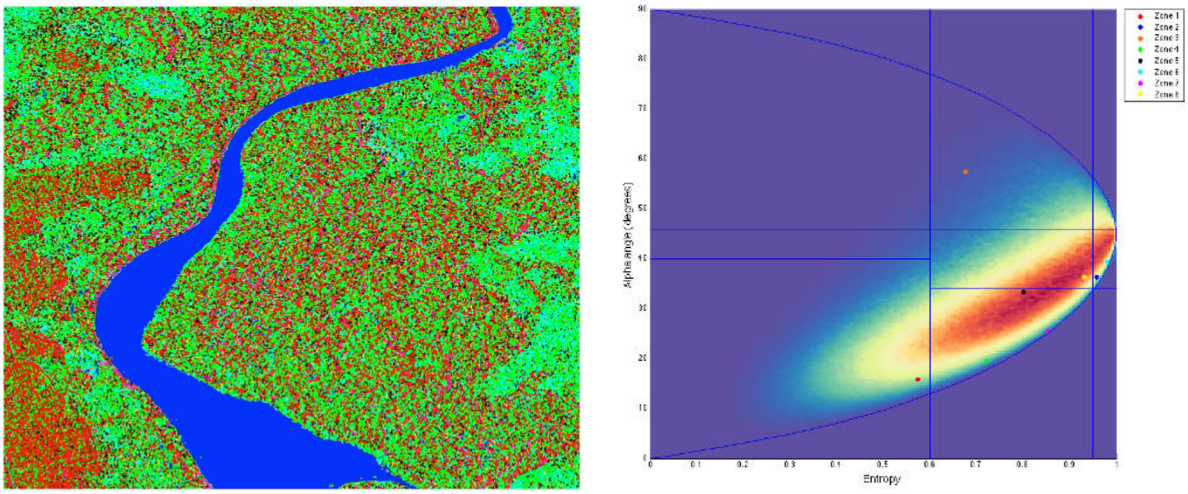

(a) (b)

Fig. 31. Second iteration of the subset A: (a) classified image, (b) cluster centers

Figure 31.a shows the result of the second iteration of the Wishart classifier. Compared with the first iteration (Figure 30.a) the forest is now much more differentiated, the zones with more sparse vegetation and dryer than the rest of the forest have been fully classified as medium entropy surface scattering, while the rest of the forest, occupying the main part of the image, has been classified combining low and medium entropy with surface scattering due to the increased density of vegetation in a uniform way.

In this second iteration the improvement regarding to the first iteration is also considerable and the termination criterion has neither been met, so the Wishart classifier is iterated again using the resulting classification as input for the third iteration. In Figure 31.b the centers of the clusters of the input to the third iteration are shown.

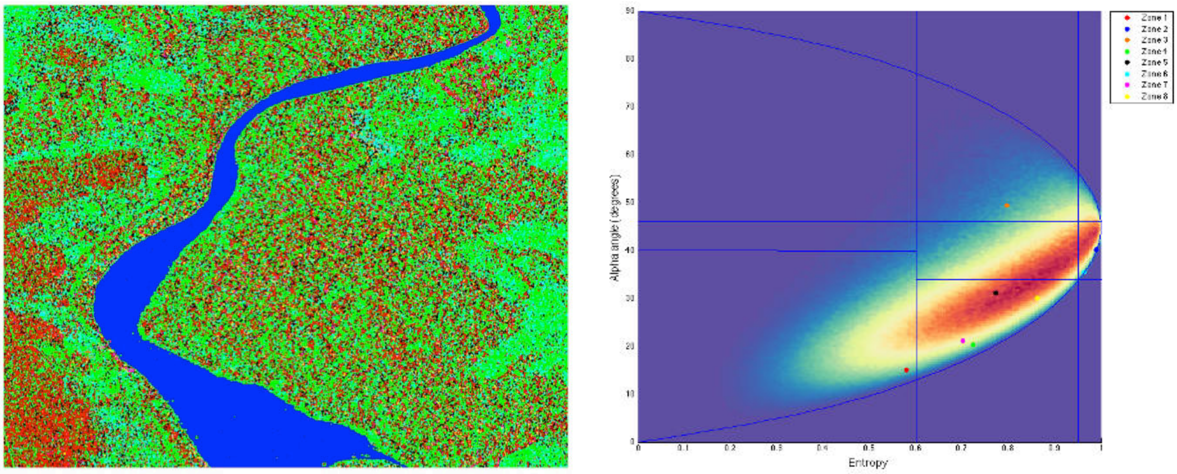

(a)

(b)

Fig. 32. Third iteration of the subset A: (a) classified image, (b) cluster centers

Figure 32.a shows the result of the third iteration of the Wishart classifier. Compared with the second iteration (Figure 31.a), the zones with low entropy surface scattering have been homogenized slightly but the image is very similar and it has not much improvement. In this case, the termination criterion has been met and the classification has ended. Comparing the final image with the first classification map obtained with the H-α plane (Figure 21) the improvement is very significant and the different zones are now much more differentiated.

- **Subset B**

The Wishart classification applied to the subset B follows the same flow diagram (Figure 28) than in the previous subset.

The cluster centers of the initial classification map of the subset B (Figure 24) are shown in Figure 33, using the density H-α plane obtained in Chapter 5.3.

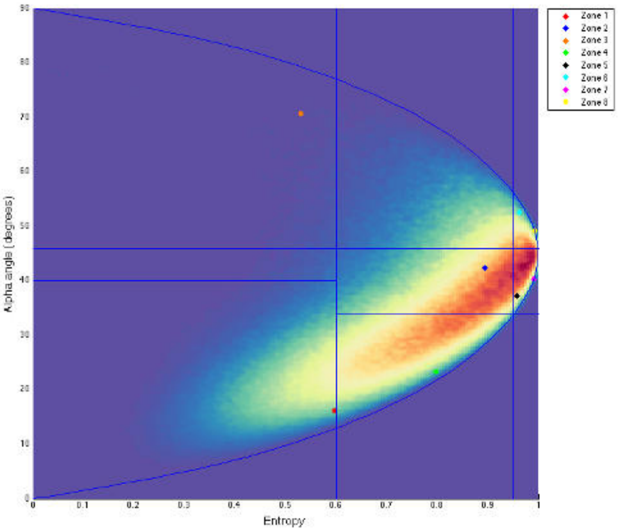

Fig. 33. Cluster centers of the initial classification map of the subset B.

The centers of the clusters are close to the region with more density of pixels and, as in the case of the subset A, the centers of the zones with less density of pixels can appear in other zones.

Once the centers of the clusters have been obtained, the Wishart distance is computed to reclassify each pixel to the cluster with lowest distance. The reclassified image of the first iteration is shown in Figure 34.a.

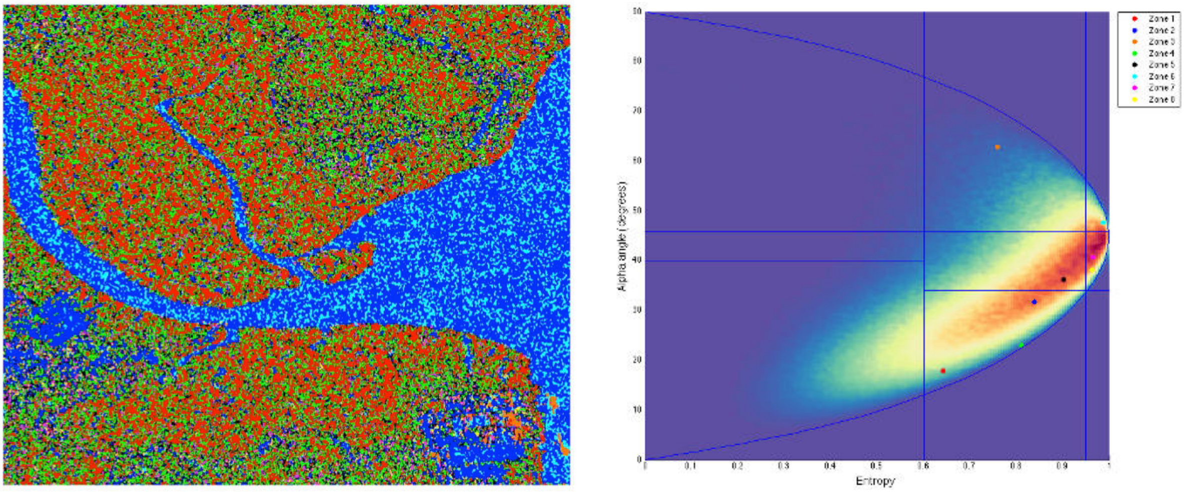

(a) (b)

Fig. 34. First iteration of the subset B: (a) classified image, (b) cluster centers

Figure 34.a shows the result of the first iteration of the Wishart classifier. Compared with the initial classification map obtained with the H-α plane (Figure 24), the river is now much more differentiated, which has been fully classified as low entropy dipole scattering. However, some parts of the image containing forests have been classified with the same class than the river, so due to the termination criterion has not been met, another iteration will be required. It is noted that in the bottom right of the image the ships and the buildings have been correctly classified as low entropy multiple scattering (in orange color).

In Figure 34.b the centers of the clusters of the input to the second iteration are shown. Those centers, as has been done previously, will be used to classify the image again (Figure 35.a) by means of the Wishart distance.

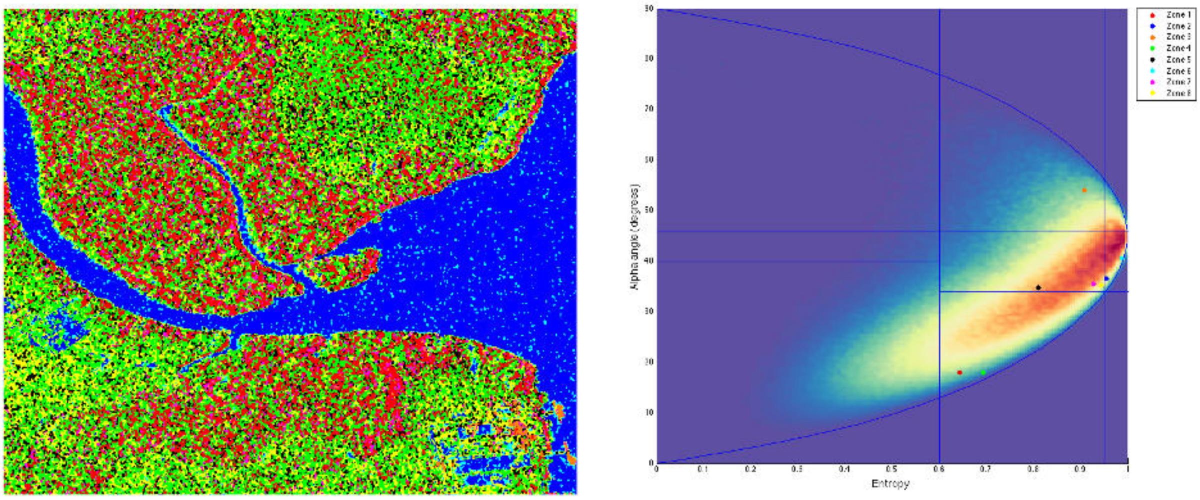

(a) (b)

Fig. 35. Second iteration of the subset B: (a) classified image, (b) cluster centers

The zones with more sparse vegetation and dryer than the rest of the forest are now much more differentiated and have been fully classified as medium entropy surface scattering, while the rest of the forest, occupying the rest of the image, has been classified combining low and medium entropy with surface scattering due to the increased density of vegetation in a uniform way. The zones classified previously with the same class than in the water are now more reduced and the zones containing buildings and ships are still correctly classified as low entropy multiple scattering.

In this second iteration the improvement regarding to the first iteration is very considerable and the termination criterion has neither been met, so another iteration of the Wishart classifier is done using the resulting classification as input for the third iteration. In Figure 35.b the centers of the clusters of the reclassified image are shown.

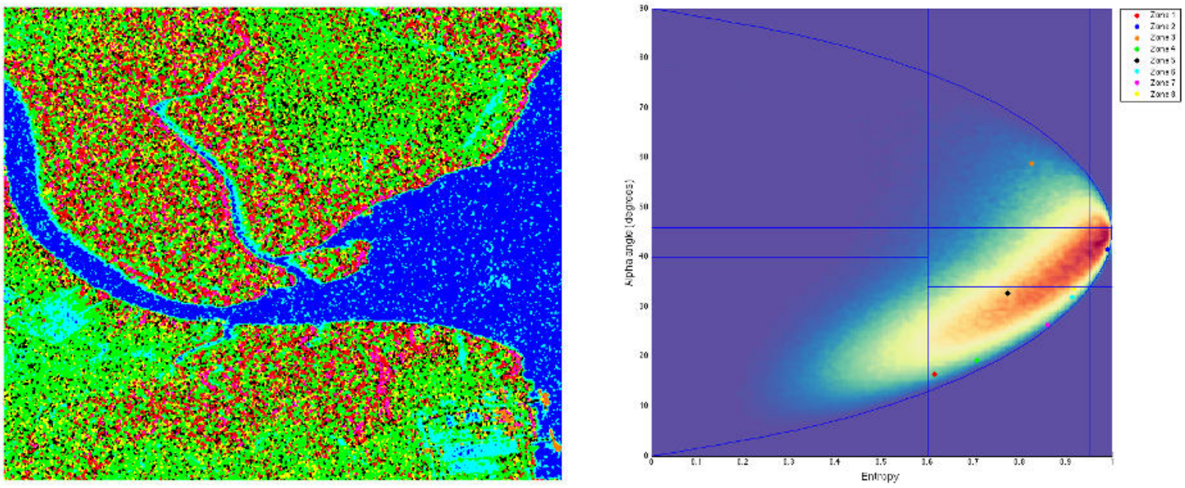

(a) **(b)**

Fig. 36. Third iteration of the subset B: (a) classified image, (b) cluster centers

Figure 36.a shows the result of the third iteration of the Wishart classifier. Compared with the second iteration (Figure 35.a), the zones that were wrongly classified as river are now classified as medium entropy multiple scattering and the zones with sparse vegetation and dryer than the rest of the forest are now slightly more differentiated. The zones containing buildings and ships (at bottom right) have been correctly classified as low entropy multiple scattering.

- **Subset C**

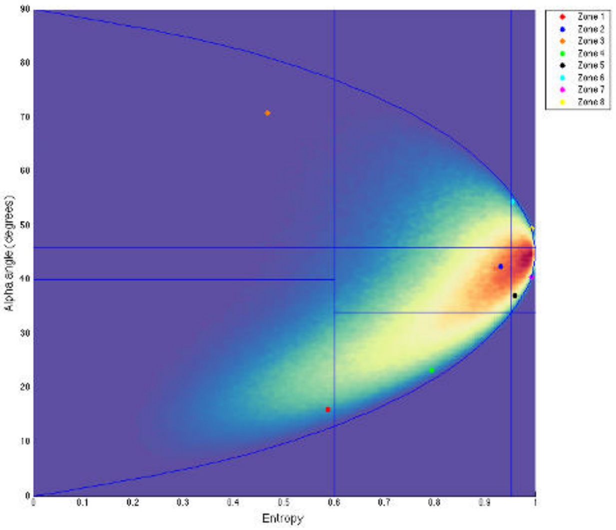

Fig. 37. Cluster centers of the initial classification map of the subset C.

According to the flow diagram of Figure 28, and as has been done in the previous subsets, the first step is the computation of the centers of the clusters of the initial classification map Figure 37. The cluster centers are close to the region with more density of pixels and in some cases leaving the area to which they correspond.

With the centers of the clusters, according to the flow diagram of the Figure 28, the Wishart distance is computed to reclassify each pixel to the cluster with lowest distance. The result of the first iteration of the Wishart classifier is shown in Figure 38.a.

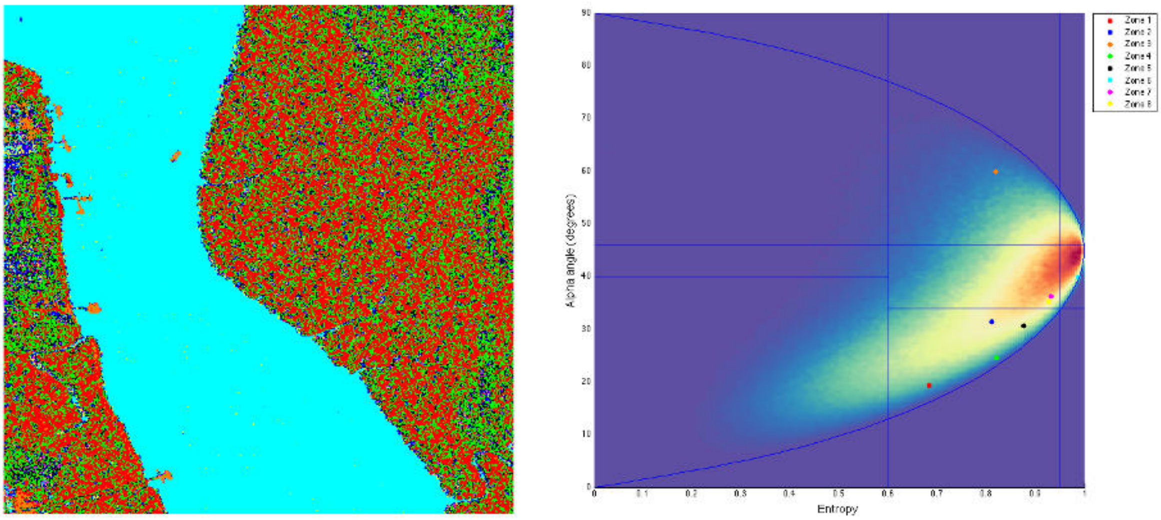

(a) (b)

Fig. 38. First iteration of the subset C: (a) classified image, (b) cluster centers

Figure 38.a shows the result of the first iteration of the Wishart classifier applied to the subset C. Compared with the initial classification map obtained with the H-α plane (Figure 27) the river is now much more differentiated, which has been fully classified as medium entropy multiple scattering. However, the zones with forest have been classified as low and medium entropy surface scattering with a lot of dispersion. It should be noted that in the river the ships and the buildings have been correctly classified as low entropy multiple scattering.

In Figure 38.b the centers of the clusters of the input to the second iteration are shown. Those centers, as has been previously done, will be used to classify the image again (Figure 39.a) by means of the Wishart distance.

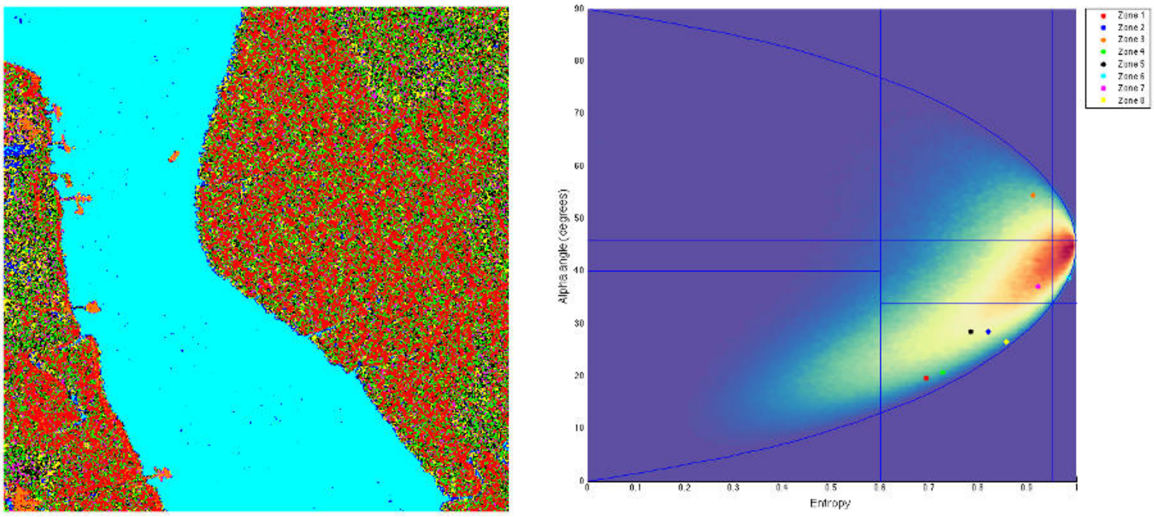

(a) **(b)**

Fig. 39. Second iteration of the subset C: (a) classified image, (b) cluster centers

The zones with forest are still classified as low and medium entropy surface scattering with a lot of dispersion, without observing any improvement. The ships and the buildings around the river are still correctly classified as low entropy multiple scattering, which means that this kind of classification can be useful for target detection.

In this case, the termination criterion has been met in the second iteration but another iteration has been done in order to see how evolve the classifier. In Figure 39.b the centers of the clusters of the reclassified image are shown.

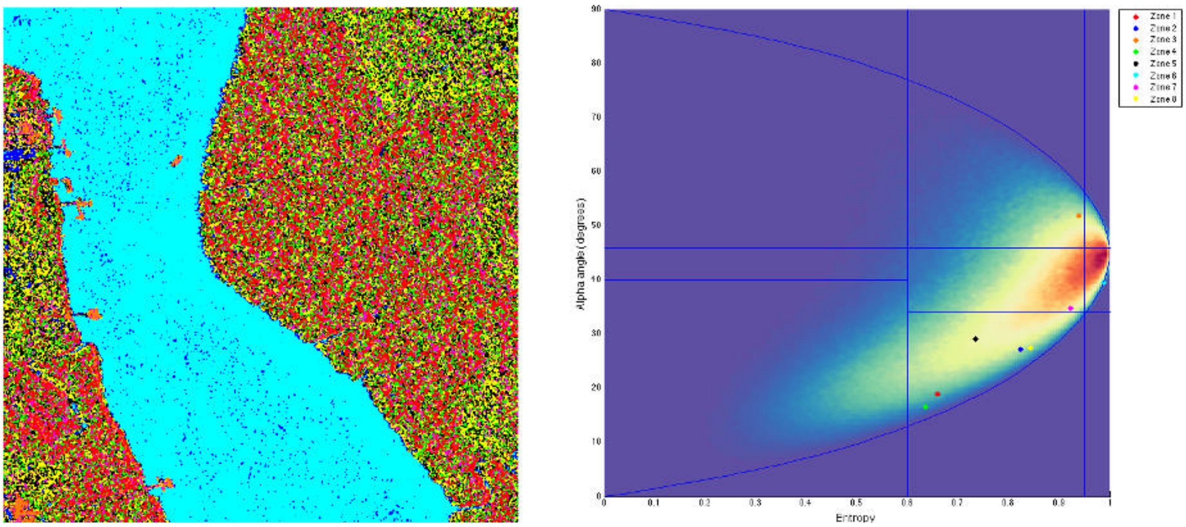

(a) **(b)**

Fig. 40. Third iteration of the subset C: (a) classified image, (b) cluster centers

Figure 40.a shows the result of the third iteration of the Wishart classifier. Compared with the second iteration (Figure 39.a) the river contains more noise and some zones of the forest are now wrongly classified as complex structures. This third iteration gives worst results than the second, so the termination criterion was correctly reached in the previous iteration.

Chapter 7

Conclusions

In this thesis the H-α decomposition method and the unsupervised Wishart classifier have been applied to a dual-polarized polarimetric Synthetic Aperture Radar (SAR) dataset using MATLAB computing environment.

It has been proved the power of the H-α decomposition method that characterizes the properties of the different types of scattering mechanism of the terrain. It has been observed that the highest values of entropy have been appeared in the river and in some areas of the forest. This is explained due to for smooth river surfaces, with little or no relief at the scale of the radar wavelength, there is little return energy as the incident wave undergoes specular reflection. These areas are associated with high alpha and high entropy, indicating that very low amplitude backscatter is mainly random noise. The lowest values of entropy and alpha have been found in the crops because they follow a more ordered and homogeneous structure.

According to the results obtained with the algorithm proposed by Lee et al., which is a combination of the unsupervised H-α decomposition classifier and the supervised Wishart classifier, it has produced very good terrain classification, especially in the water that has been segmented in a uniform way. While iterating, the centers of the cluster were closer to the region with more density of pixels and often changing its zone. Finally, it has been proved that approximately after three iterations the results were stabilized and the termination criterion was reached.

Although the full-polarization SAR data have more physical scattering information about the targets, it has been proved that the dual-polarized SAR data provides enough scattering information of the objective to generate good classification results with much lower computational cost. It can be conclude that dual-polarized data can be a good alternative to full-polarization data, which requires high size of data and strong constraints in the data acquisition system.

References

[1] Kent, S., Ucan, O. N. and Ensari, T., "Speckle Reduction of Synthetic Aperture Radar Images Using Wavelet Filtering" *5th European Conf. on Synthetic Aperture Radar, EUSAR,* Ulm, GERMANY, 25-27 May 2004, 1001-1004.

[2] Sugimoto, M., and K. Ouchi. "Extraction of Laver Cultivation Area Using SAR Dual Polarization Data." *PIERS Proceedings, Moscow, Russia*, 2012.

[3] Bourgeau-Chavez, L. L., Leblon, B., Charbonneau, F. and Buckley, J. R., "Evaluation of Polarimetric Radarsat-2 SAR Data for Development of Soil Moisture Retrieval Algorithms over a Chronosequence of Black Spruce Boreal Forests." *Remote Sensing of Environment*, 2013, 71-85.

[4] Chan, Y. K. and Koo, V. C., "An Introduction To Synthetic Aperture Radar (SAR)" *Progress In Electromagnetics Research B*, 2008, 27-60.

[5] Tedesco, M., *Remote Sensing of the Cryosphere*. John Wiley & Sons, 2014. 12.

[6] Lee, J. S. and Pottier, E., *Polarimetric Radar Imaging: From Basics to Applications*. Boca Raton: CRC Press, 2009.

[7] Kim, A. J., Krim, A. H. and Willsky, A. S., "Segmentation-directed SAR image compression via hierarchical stochastic modeling" *AeroSense'97. International Society for Optics and Photonics, 1997,* 386-397.

[8] Atlantis Scientific Inc., "Theory of Synthetic Aperture Radar", 1997. Accessed November 8, 2014. http://www.geo.uzh.ch/~fpaul/sar_theory.html.

[9] Maini, A. K., and Agrawal, V., *Satellite Technology Principles and Applications*. 3rd ed. Chichester, West Sussex, U.K.: John Wiley & Sons, 2014. 11-15.

[10] Lakhankar, T., *Estimation of Soil Moisture Using Microwave Remote Sensing Data.* City University of New York, ProQuest, 2006.

[11] Abid, M. M., *Spacecraft Sensors*. Chichester, West Sussex, England: John Wiley & Sons, 2005. 274.

[12] Knee, P., *Sparse Representations for Radar with MATLAB® Examples*. San Rafael,

Calif. (1537 Fourth Street, San Rafael, CA 94901 USA): Morgan & Claypool, 2012. 36.

[13] Khwaja, S., *Fast Raw Data Generation of Realistic Environments for a SAR System Simulator*. Signal and Image processing. Université Rennes 1, 2008.

[14] Reddy, M. A. *Textbook of Remote Sensing and Geographical Information Systems*. 3rd ed. Hyderabad: BS Publications, 2008. 115.

[15] Mahafza, B. R., *Radar Systems Analysis and Design Using MATLAB*. 2nd ed. Boca Raton, FL: Chapman & Hall/CRC, 2005. 534.

[16] UCL Department Of Geography, "Synthetic Aperture Radar (SAR) Summary" Accessed November 30, 2014. http://www2.geog.ucl.ac.uk/~mdisney/teaching/PPRS/PPRS_7/sar_summary.pdf.

[17] Kramer, H. J. *Observation of the Earth and Its Environment: Survey of Missions and Sensors*. 2nd ed. Berlin: Springer-Verlag, 1994. 1252.

[18] Herrmann, J. and González Bottero, A., "TerraSAR-X Mission: The New Generation in High Resolution Satellites." *Simpósio Brasileiro De Sensoriamento Remoto*, 2007, 7063-070.

[19] Christian, W., "*Radar Basics.*" Radar Tutorial. Accessed December 2, 2014. http://www.radartutorial.eu/20.airborne/ab08.en.html.

[20] Roth, A., Eineder, M. and Schättler, B., "TerraSAR-X: A New Perspective For Applications Requiring High Resolution Spaceborne Sar Data." *Commission VI, WG VI/4*.

[21] Mohanakumar, K. *Stratosphere Troposphere Interactions an Introduction*. New York: Springer, 2008.

[22] Neill, S. *Electronic Warfare and Radar Systems Engineering Handbook*. S.l.: Military Bookshop, 2013. 3-2.1.

[23] Christian, W., "Radar Basics." Polarisation of Electromagnetic Waves. Accessed December 5, 2014. http://www.radartutorial.eu/06.antennas/Polarization.en.html.

[24] Bakshi, U. A., and Bakshi, A. V., *Electromagnetic Fields*. Pune, India: Technical Publications, 2010. 40.

[25] E. Collett, "*Field Guide to Polarization*", SPIE Press, Bellingham, WA (2005).

[26] Mcnairn, H., Duguay, C., Brisco, B. and Pultz, T.j, "The Effect of Soil and Crop Residue Characteristics on Polarimetric Radar Response." *Remote Sensing of Environment*: 308-20.

[27] Natural Resources Canada, "Polarization in Radar Systems." November 13, 2014.

Accessed December 23, 2014. http://www.nrcan.gc.ca/earth-sciences/geomatics/satellite-imagery-air-photos/satellite-imagery-products/educational-resources/9567.

[28] Tso, B., and Mather, P. M., *Classification Methods for Remotely Sensed Data*. 2nd ed. Boca Raton: CRC Press, 2009. 32.

[29] Karathanassi, V., and Dabboor, M., "Land Cover Classification Using E-Sar Polarimetric Data" Laboratory of Remote Sensing, School of Rural and Surveying Engineering, National Technical University of Athens, *Commission VII, WG VII/3*, 2003.

[30] Cloude, S.r., and Pottier, E., "A Review of Target Decomposition Theorems in Radar Polarimetry." *IEEE Transactions on Geoscience and Remote Sensing* 34, no. 2 (1996).

[31] Sugimoto, M. "SAR Image Analysis and Target Detection Utilizing Polarimetric Information." *National Defense Academy Graduate School of Science and Engineering*, 2013.

[32] DLR - Earth Observation. "TerraSAR-X - Germany's Radar Eye in Space." July 8, 2009. Accessed December 30, 2014. http://www.dlr.de/eo/en/desktopdefault.aspx/tabid-5725/9296_read-15979/.

[33] Ley, W. *Handbook of Space Technology*. Vol. 22. Chichester, U.K.: John Wiley & Sons, 2009.

[34] Jung, H., W. Lee, and L. Zhang. "Theoretical Accuracy of Along-Track Displacement Measurements from Multiple-Aperture Interferometry (MAI)." Sensors (Basel, Switzerland). September 23, 2014. Accessed December 29, 2014. http://www.ncbi.nlm.nih.gov/pmc/articles/PMC4208245/.

[35] LTDP Working Group. "Long Term Preservation Of Earth Observation Space Data" *European Earth Observation Space Data Set*, no. 2 (2013). Accessed December 29, 2014.

[36] Gurreonero Robinson, D. "Analysis and Evaluation in Shoreline Detection in the South Holland Province, Using Images in Quad Polarization Mode from TerraSAR-X." *Faculty of Geo-Information Science and Earth Observation of the University of Twente*, 2011.

[37] Airbus Defence and Space. "TerraSAR-X Image Product Guide." *Basic and Enhanced Radar Satellite Imagery*, no. 2 (2014).

[38] Buckreuss, S. and Schattler, B., "The TerraSAR-X Ground Segment." *IEEE Transactions on Geoscience and Remote Sensing*, no. 1.3 (2007): 623-32.

[39] Penta, B., A. O. Varghese, K. Nageswara Rao, and A. K. Joshi. "Analysis of Synthetic Aperture Radar Polarimetric Decomposition Methods for Land Cover Interpretation." *Conference: ISRS and ISG National Symposium on Remote Sensing and GIS for Environment with Special Emphasis on Marine and Coastal Dynamics, At Vishakhapattanam, India*, 2013.

[40] Zhang, L., Zhang, J., Zou, B. and Zhang, Y., "Comparison of Methods for Target Detection and Applications Using Polarimetric SAR Image." *Harbin Institute of Technology, No. 92 West Dazhi Street, Harbin 150001, China* 4, no. 1 (2008).

[41] Theodoridis, S. and Chellappa, R., *Academic Press Library in Signal Processing Communications and Radar Signal Processing.* Vol. 2. Burlington: Elsevier Science, 2013.

[42] Sakshaug, S. E., *Evaluation of Polarimetric SAR Decomposition methods for tropical forest analysis*, Faculty Of Science And Technology, University of Tromsø, 2013

[43] Turkar, V. and Rao, Y. S., "Supervised and Unsupervised Classification of PolSAR Images from SIR-C and ALOS/PALSAR Using PolSARPro." *Conference: Geomatrix'09, At Mumbai, India* CSRE, IIT Bombay (2009).

[44] Kang, M. K., Kim, K. E., Cho, S. J., Lee, H. L. and Lee, J. H., "Filtering Effect in Supervised Classification of Polarimetric Ground Based SAR Images." *Korean Journal of Remote Sensing* 26, no. 6 (2010): 705-719.

[45] Chen, C. H. *Image Processing for Remote Sensing*. Boca Raton: CRC Press/Taylor & Francis Group, 2008. 31.

[46] Ferro-Famil, L., Pottier, E. and Lee, J. S., "Unsupervised Classification of Multifrequency and Fully Polarimetric SAR Images Based on the H/A/Alpha-Wishart Classifier." *IEEE Transactions on Geoscience and Remote Sensing* 39, no. 11 (2002): 2332-342.